Title

Structural and functional human retinal imaging with a fiber-based visible light OCT ophthalmoscope.

Journal

Biomedical Optics Express, 8(1)

ISSN

2156-7085

Authors

Chong, Shau Poh
Bernucci, Marcel
Radhakrishnan, Harsha
et al.

Publication Date

2017

DOI

10.1364/boe.8.000323

Peer reviewed

Research Article | Vol. 8, No. 1 | 1 Jan 2017 | BIOMEDICAL OPTICS EXPRESS 323

Biomedical Optics EXPRESS

Structural and functional human retinal imaging with a fiber-based visible light OCT ophthalmoscope

Shau Poh Chong,[1] Marcel Bernucci,[1] Harsha Radhakrishnan,[1] and Vivek J. Srinivasan[1,2,*]

[1]*Biomedical Engineering Department, University of California Davis, Davis, California 95616, USA*
[2]*Department of Ophthalmology and Vision Science, University of California Davis School of Medicine, Sacramento, California 95817, USA*
[*]*vjsriniv@ucdavis.edu*

Abstract: The design of a multi-functional fiber-based Optical Coherence Tomography (OCT) system for human retinal imaging with < 2 micron axial resolution in tissue is described. A detailed noise characterization of two supercontinuum light sources with different pulse repetition rates is presented. The higher repetition rate and lower noise source is found to enable a sensitivity of 96 dB with 0.15 mW light power at the cornea and a 98 microsecond exposure time. Using a broadband (560 ± 50 nm), 90/10, fused single-mode fiber coupler designed for visible wavelengths, the sample arm is integrated into an ophthalmoscope platform, similar to current clinical OCT systems. To demonstrate the instrument's range of operation, *in vivo* structural retinal imaging is also shown at 0.15 mW exposure with 10,000 and 70,000 axial scans per second (the latter comparable to commercial OCT systems), and at 0.03 mW exposure and 10,000 axial scans per second (below maximum permissible continuous exposure levels). Lastly, *in vivo* spectroscopic imaging of anatomy, saturation, and hemoglobin content in the human retina is also demonstrated.

OCIS codes: (170.3880) Optical coherence tomography; (170.6480) Medical and biological imaging; (170.6480) Spectroscopy, speckle; (060.2350) Fiber optics imaging; (140.7300) Visible lasers.

References and links

1. M. Wojtkowski, R. Leitgeb, A. Kowalczyk, T. Bajraszewski, and A. F. Fercher, "In vivo human retinal imaging by Fourier domain optical coherence tomography," J. Biomed. Opt. **7**, 457–463 (2002).
2. J. S. Schuman, C. A. Puliafito, J. G. Fujimoto, and J. S. Duker, *Optical Coherence Tomography of Ocular Diseases*, 3rd ed. (SLACK Inc., Thorofare, NJ, 2013), pp. xviii, 615.
3. E. C. W. Lee, J. F. de Boer, M. Mujat, H. Lim, and S. H. Yun, "In vivo optical frequency domain imaging of human retina and choroid," Opt. Express **14**, 4403–4411 (2006).
4. R. Leitgeb, C. Hitzenberger, and A. Fercher, "Performance of fourier domain vs. time domain optical coherence tomography," Opt. Express **11**, 889–894 (2003).
5. J. F. de Boer, B. Cense, B. H. Park, M. C. Pierce, G. J. Tearney, and B. E. Bouma, "Improved signal-to-noise ratio in spectral-domain compared with time-domain optical coherence tomography," Opt. Lett. **28**, 2067–2069 (2003).
6. M. Choma, M. Sarunic, C. Yang, and J. Izatt, "Sensitivity advantage of swept source and Fourier domain optical coherence tomography," Opt. Express **11**, 2183–2189 (2003).
7. B. R. White, M. C. Pierce, N. Nassif, B. Cense, B. H. Park, G. J. Tearney, B. E. Bouma, T. C. Chen, and J. F. de Boer, "In vivo dynamic human retinal blood flow imaging using ultra-high-speed spectral domain optical Doppler tomography," Opt. Express **11**, 3490 (2003).
8. C. Xu, C. Vinegoni, T. S. Ralston, W. Luo, W. Tan, and S. A. Boppart, "Spectroscopic spectral-domain optical coherence microscopy," Opt. Lett. **31**, 1079–1081 (2006).
9. J. Yi, Q. Wei, W. Liu, V. Backman, and H. F. Zhang, "Visible-light optical coherence tomography for retinal oximetry," Opt. Lett. **38**, 1796–1798 (2013).
10. S. Makita, Y. Hong, M. Yamanari, T. Yatagai, and Y. Yasuno, "Optical coherence angiography," Opt. Express **14**, 7821–7840 (2006).
11. J. Fingler, D. Schwartz, C. H. Yang, and S. E. Fraser, "Mobility and transverse flow visualization using phase variance contrast with spectral domain optical coherence tomography," Opt. Express **15**, 12636–12653 (2007).
12. R. K. Wang, S. L. Jacques, Z. Ma, S. Hurst, S. R. Hanson, and A. Gruber, "Three dimensional optical angiography," Opt. Express **15**, 4083–4097 (2007).
13. A. Unterhuber, B. Povazay, B. Hermann, H. Sattmann, A. Chavez-Pirson, and W. Drexler, "In vivo retinal optical coherence tomography at 1040 nm-enhanced penetration into the choroid," Opt. Express **13**, 3252–3258 (2005).

#278483 http://dx.doi.org/10.1364/BOE.8.000323
Journal © 2017 Received 10 Oct 2016; revised 13 Dec 2016; accepted 13 Dec 2016; published 19 Dec 2016

Biomedical Optics EXPRESS

14. X. R. Huang, Y. Zhou, W. Kong, and R. W. Knighton, "Reflectance Decreases before Thickness Changes in the Retinal Nerve Fiber Layer in Glaucomatous Retinas," Invest. Ophth. Vis. Sci. **52**, 6737–6742 (2011).
15. F. E. Robles, C. Wilson, G. Grant, and A. Wax, "Molecular imaging true-colour spectroscopic optical coherence tomography," Nat. Photon. **5**, 744–747 (2011).
16. R. N. Pittman, "In vivo photometric analysis of hemoglobin," Ann. Biomed. Eng. **14**, 119–137 (1986).
17. S. P. Chong, C. Merkle, H. Radhakrishnan, C. Leahy, A. Dubra, Y. Sulai, and V. J. Srinivasan, "Optical Coherence Imaging of Microvascular Oxygenation and Hemodynamics," in CLEO: 2014, OSA Technical Digest (online) (Optical Society of America, 2014), ATh1O.2.
18. S. P. Chong, C. W. Merkle, C. Leahy, H. Radhakrishnan, and V. J. Srinivasan, "Quantitative microvascular hemoglobin mapping using visible light spectroscopic Optical Coherence Tomography," Biomed. Opt. Express **6**, 1429–1450 (2015).
19. B. Povazay, K. Bizheva, A. Unterhuber, B. Hermann, H. Sattmann, A. F. Fercher, W. Drexler, A. Apolonski, W. J. Wadsworth, J. C. Knight, P. S. Russell, M. Vetterlein, and E. Scherzer, "Submicrometer axial resolution optical coherence tomography," Opt. Lett. **27**, 1800–1802 (2002).
20. J. Yi, S. Y. Chen, X. Shu, A. A. Fawzi, and H. F. Zhang, "Human retinal imaging using visible-light optical coherence tomography guided by scanning laser ophthalmoscopy," Biomed. Opt. Express **6**, 3701–3713 (2015).
21. J. J. Hunter, J. I. Morgan, W. H. Merigan, D. H. Sliney, J. R. Sparrow, and D. R. Williams, "The susceptibility of the retina to photochemical damage from visible light," Prog. Retin. Eye Res. **31**, 28–42 (2012).
22. "ANSI Z136.1 American National Standard for Safe Use of Lasers," (Laser Institute of America, 2014).
23. W. J. Brown, S. Kim, and A. Wax, "Noise characterization of supercontinuum sources for low-coherence interferometry applications," J. Opt. Soc. Am. A. **31**, 2703–2710 (2014).
24. V. J. Srinivasan, R. Huber, I. Gorczynska, J. G. Fujimoto, J. Y. Jiang, P. Reisen, and A. E. Cable, "High-speed, high-resolution optical coherence tomography retinal imaging with a frequency-swept laser at 850 nm," Opt. Lett. **32**, 361–363 (2007).
25. S. Makita, T. Fabritius, and Y. Yasuno, "Full-range, high-speed, high-resolution 1-μm spectral-domain optical coherence tomography using BM-scan for volumetric imaging of the human posterior eye," Opt. Express **16**, 8406–8420 (2008).
26. F. C. Delori, R. H. Webb, and D. H. Sliney, "Maximum permissible exposures for ocular safety (ANSI 2000), with emphasis on ophthalmic devices," J. Opt. Soc. Am. A **24**, 1250–1265 (2007).
27. K. L. Corwin, N. R. Newbury, J. M. Dudley, S. Coen, S. A. Diddams, K. Weber, and R. S. Windeler, "Fundamental noise limitations to supercontinuum generation in microstructure fiber," Phys. Rev. Lett. **90**, 113904 (2003).
28. U. Moller, S. T. Sorensen, C. Larsen, P. M. Moselund, C. Jakobsen, J. Johansen, C. L. Thomsen, and O. Bang, "Optimum PCF tapers for blue-enhanced supercontinuum sources," Opt. Fiber Technol. **18**, 304–314 (2012).
29. M. Wojtkowski, V. Srinivasan, T. Ko, J. Fujimoto, A. Kowalczyk, and J. Duker, "Ultrahigh-resolution, high-speed, Fourier domain optical coherence tomography and methods for dispersion compensation," Opt. Express **12**, 2404–2422 (2004).
30. V. J. Srinivasan, D. C. Adler, Y. Chen, I. Gorczynska, R. Huber, J. S. Duker, J. S. Schuman, and J. G. Fujimoto, "Ultrahigh-Speed Optical Coherence Tomography for Three-Dimensional and En Face Imaging of the Retina and Optic Nerve Head," Invest. Ophth. Vis. Sci. **49** (11), 5103–5110 (2008).
31. C. Kasai, K. Namekawa, A. Koyano, and R. Omoto, "Real-time two-dimensional blood flow imaging using an autocorrelation technique," IEEE Trans. Sonics Ultrason. **32**(3), 458–464 (1985).
32. "MedlinePlus Medical Encyclopedia: RBC Indices" (Last updated on 13th March 2016), retrieved 06th Oct, 2016, https://medlineplus.gov/ency/article/003648.htm.
33. R. W. Knighton, X. Huang, and Q. Zhou, "Microtubule contribution to the reflectance of the retinal nerve fiber layer," Invest. Ophth. Vis. Sci. **39**, 189–193 (1998).
34. D. J. Faber, M. C. G. Aalders, E. G. Mik, B. A. Hooper, M. J. C. van Gemert, and T. G. van Leeuwen, "Oxygen saturation-dependent absorption and scattering of blood," Phys. Rev. Lett. **93**(2), 028102 (2004).
35. N. V. Iftimia, D. X. Hammer, C. E. Bigelow, D. I. Rosen, T. Ustun, A. A. Ferrante, D. Vu, and R. D. Ferguson, "Toward noninvasive measurement of blood hematocrit using spectral domain low coherence interferometry and retinal tracking," Opt. Express **14**, 3377–3388 (2006).
36. T. W. Secomb, "Blood Flow in the Microcirculation," Annu. Rev. Fluid Mech. **49** (1) (2016).

1. Introduction

Over the past decade, advances in high-speed, high-resolution Fourier domain Optical Coherence Tomography (FDOCT) for human retinal and optic nerve head imaging [1] have improved the diagnosis and monitoring of major eye diseases [2]. For a given light exposure level and imaging speed, FDOCT methods, including spectral-domain (SD) OCT [1] and swept-source (SS) OCT [3], provide a > 20 dB increase in sensitivity compared to time-domain OCT [4–6], thus enabling faster imaging speed. The Fourier domain detection scheme also provides access to both amplitude and phase of the complex OCT signal, facilitating Doppler [7], spectroscopic [8, 9],

Biomedical Optics EXPRESS

and angiographic imaging [10–12]. SDOCT systems that operate at 800 nm currently dominate the clinical ophthalmology market due to their low cost and high resolution. Wavelengths around 1050 nm [3, 13] experience less scattering in ocular tissues, and can be used to image deeper into the optic nerve and choroid. However, the narrow water absorption window around 1050 nm may limit the achievable axial resolution in the human eye.

While OCT at 800 nm and 1050 nm enables excellent tissue architectural contrast, visible light is more sensitive to absorption from chromophores such as photopigment, melanin, and hemoglobin, as well as scattering from subcellular structures [14], all of which are potential retinal disease biomarkers. Recently, intense and broadband supercontinuum (SC) light sources have made it possible to perform OCT in the visible wavelength regime [9, 15]. Due to higher hemoglobin absorption [16], visible light OCT enables quantitative measurement [9, 15] and mapping [17, 18] of hemoglobin concentrations. Another intrinsic advantage of visible light OCT is higher axial resolution for a given wavelength bandwidth [19]. To date, most high-resolution visible light OCT systems [18, 20] have adopted free-space, or bulk, optical setups. This is mainly due to the challenges of achieving broad bandwidth, high efficiency, and dispersion management in an all-fiber system. However, the large footprint and frequent alignment required for bulk optical systems [20] could limit clinical applications. Moreover, the use of visible light for OCT requires additional safety considerations. The blue light hazard limits maximum permissible exposure [21, 22]. In addition, higher absorption and scattering of ocular tissues at visible wavelengths limit achievable imaging depths. These challenges are compounded by the fact that SC light sources typically introduce significant amounts of excess noise [23].

Here we present a fiber-based visible light OCT system for high-resolution *in vivo* human retinal imaging. The prototype system is built on an ophthalmoscope platform, similar to existing commercial clinical OCT instruments. Excess noise levels are characterized in detail for two SC light sources with different pulse repetition rates. The optimal reference power level and achievable sensitivity are identified for each light source and exposure period. Using operating regimes deemed to be optimal, fiber-based visible light OCT imaging of the human retina with < 2 μm axial resolution in tissue is demonstrated at a range of incident powers and speeds. High-resolution spectroscopic layer-by-layer comparisons of reflectance, as well as hemoglobin saturation and concentration mapping in retinal vessels, are demonstrated.

2. Methods

2.1. System design and spectrometer calibration

A high-speed, fiber-based visible light spectral/Fourier domain OCT system (Fig. 1(A)) was constructed for *in vivo* imaging of the human retina. The system used an unpolarized low-noise SC light source (SuperK EXU3, NKT Photonics) with a collimated output beam. The output beam of ~ 600 μm diameter at visible wavelengths was first attenuated by 91% via reflection from a sapphire window and spectrally filtered to center the spectrum at 575 nm. Then, the collimated, filtered beam was coupled into the input port of a 560 ± 50 nm, 460-HP fiber coupler with a 90/10 splitting ratio. The 90/10 coupler was used to maximize the coupling of backscattered light from the sample to the detection port. One output port of the fiber was connected to the sample arm, which was integrated into an ophthalmoscope platform (Fig. 1(B)), rendering it compact. The broadband coupler performance was also verified using the SC light source (Fig. 1(C)). In the sample arm, the 10% output port of the coupler was collimated using an achromatic doublet (f = 10 mm). The collimated beam (~2 mm in diameter) was raster scanned by a 2D galvanometer scanner (CTI 6210H, Cambridge Technology) before being magnified/de-magnified by a quasi-telecentric beam expander/compressor, consisting of two achromatic doublets pairs with effective focal lengths of 37.5 mm and 50 mm. Two configurations, with magnifications of 1.33 and 0.75 from the galvanometers to the pupil, were tested. The first configuration with larger magnification allowed for an angular field-of-view (FOV) of 25°. The second configuration with

Biomedical Optics EXPRESS

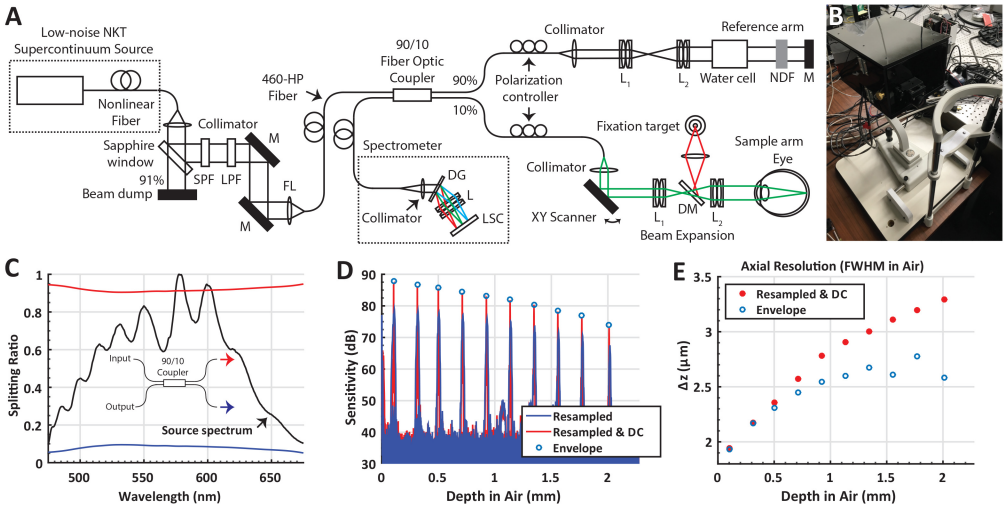

Fig. 1. Fiber-based visible light OCT system for imaging the human retina. (A). Light from the supercontinuum light source passed through a short-pass filter (SPF) and a long-pass filter (LPF) after ~9% reflection by a sapphire window before fiber coupling. A dichroic mirror was used to image a fixation target illuminated by a red LED onto the subject's retina. M: mirror; L: lens; FL: focusing lens; DG: diffraction grating; LSC: line-scan camera, NDF: neutral density filter, DM: dichroic mirror. (B) A photograph showing the sample arm (covered) mounted on the ophthalmoscope platform. (C) The splitting ratio (90% arm-red, 10% arm-blue) of the broadband fiber coupler was measured using the OCT spectrometer, demonstrating flatness across the source spectrum (black). The FWHM spectral bandwidth was ~110 nm. Assuming a Gaussian spectrum led to an axial resolution (FWHM of point spread function) of ~1.4 μm in air. The spectrometer configuration used for imaging spanned ~151 nm over 4096 pixels. Direct Fourier transformation of the spectrum registered on the spectrometer yielded an axial resolution of ~1.7 μm in air. (D) The sensitivity rolloff, estimated from point spread functions (PSFs), derived by Fourier transformation of the resampled and dispersion compensated (DC) spectral fringes, was ~5-6 dB over the first half of the axial imaging range. Dispersion mismatch caused significant PSF broadening (blue), but if compensated (red), PSFs approached the sensitivity rolloff determined by Fourier transformation of the resampled spectral fringe envelopes [24] (blue circles). (E) The measured axial FWHM resolution was < 2.1 μm (in tissue) over the first half of the axial range.

Biomedical Optics EXPRESS

smaller magnification increased the angular FOV to 40°. The light in the reference arm traversed the same lenses as in the sample arm. A variable neutral density filter (NDF) was used to adjust the reference power and a 20 mm water cell was placed in the beam path for dispersion balancing during retinal imaging.

The back-reflected beams from both arms were combined in the output coupler port and directed to a custom-made spectrometer. The light from the output fiber was collimated using a 50 mm achromatic doublet. A volume transmission grating (1800 lines per millimeter, Wasatch Photonics) dispersed the light, which was focused by a lens (achromatic doublet pair with an effective focal length of 125 mm) onto a complementary metal-oxide semiconductor (CMOS) line-scan camera (Basler SPL 4096-140km). Vertical binning mode was used and the output mode of the camera was set to 12-bit. All of the achromats were purchased from Thorlabs, Inc. In contrast to our previous work [17, 18], the spectrometer was designed to use the full 4096-pixel acquisition window of the line scan camera, enabling a line rate up to 70 kHz. The sensitivity rolloff of the system was measured to be ~5-6 dB over the first half of the axial imaging range (Fig. 1(D)) while the axial resolution varied from ~1.4-2.1 μm in tissue over the first half of the axial imaging range (Fig. 1(E)). The maximum sensitivity was measured after accounting for 40 dB attenuation in the sample arm with an OD 2.0 neutral density filter.

At shorter wavelengths in the visible light spectrum, attenuation in the 460-HP fiber increased and aluminum mirror reflectivity decreased. The sensitivity loss caused by galvanometer mirror reflections is a particular concern due to the double-pass geometry. We tested higher efficiency dielectric mirrors, which enabled higher system sensitivity, but polarization mode dispersion associated with the dielectric mirrors was challenging to compensate numerically, even when matched dielectrics were placed in the reference arm. Therefore, images using the dielectric mirrors are not shown here. The system/acquisition configurations as well as the measured system performance, for each imaging configuration, are summarized in Table 2.1.

Table 1. System configuration and measured parameters.

System/acquisition configuration	I	II	III	IV
Axial scan rate (Hz)	10,000	10,000	10,000	70,000
Incident power at cornea (μW)	100	30	150	150
Maximum sensitivity (dB)	94	89	96	87
Beam diameter at cornea (mm)	2.8	1.6	1.6	1.6
Angular FOV (°)	25	40	40	40

To perform spectroscopy, the spectrometer was calibrated as previously described [18, 25]. Briefly, spectral interference fringes from a mirror were acquired at two distinct distances, each well-separated from the zero delay. The corresponding spectral phases were obtained through Hilbert transformation and the spectral phase difference was fitted using a tenth-order polynomial function. Using two laser diodes with known wavelengths, and prior knowledge of the path length difference between the two spectral interference measurements, the fitted spectral phase difference was converted to a corresponding pixel-specific wavenumber function. The calibrated wavenumber function was then used to resample the OCT interference fringes to be evenly spaced in wavenumber, and to assign wavenumbers to depth-resolved spectra. The calibrated spectral sampling interval of the system was ~0.037 nm, which provided an imaging depth of 2.24 mm, or 1.1 μm per pixel in air. The camera was connected to a frame grabber (PCIe-1433, National Instruments), and triggered by a digital I/O board (PCIe-6351, National Instruments), which also controlled the 2D galvanometer scanner. Acquisition was synchronized by a custom LabVIEW program that displayed cross-sectional OCT images in real-time, using different scanning patterns at a range of acquisition rates.

Biomedical Optics EXPRESS

2.2. Light safety considerations

Light exposure can damage the retina through photothermal, photomechanical, and photochemical mechanisms [26]. Due to the normal dispersion induced by propagation in the single mode fiber (460-HP), the already normally dispersed pulse from the photonic crystal fiber was stretched to the nanosecond scale. Thus, the incident light can be considered as quasi-continuous wave and photomechanical effects can be neglected. Photochemical considerations limit maximum permissible exposure (MPE) at shorter wavelengths for longer exposures, while photothermal effects limit MPE at longer wavelengths for shorter exposures. Based on the newest ANSI Z136.1 - 2014 American National Standard for Safe Use of Lasers published by Laser Institute of America [22], the MPE was determined for both a stationary point source (yielding the most conservative estimates) for 0.5 seconds, and a line or area scanning laser, treated as extended sources, for a duration of 10 seconds. For wavelengths from 400 nm to 700 nm (Fig. 1(C)), and a beam diameter of 3 mm at the cornea, the MPE was estimated to be 150 μW for a stationary beam for an exposure duration of 0.5 seconds. Nevertheless, for an extreme case of 8 hours "continuous" exposure, the MPE is 70 μW for a wavelength range of 500 - 700 nm. The MPE for 550 nm line illumination (corresponding to a line scan) subtending an angle of 17° was estimated to be 2.15 mW for an exposure duration of 10 seconds. Using similar assumptions, the MPE for 550 nm area illumination (corresponding to a raster scan) covering an angular field of view of 17° by 17° was estimated to be 7.07 mW for the same exposure duration. For the current study, the average power delivered to the cornea for retinal image acquisition was 100 - 150 μW, consistent with the MPE calculations above. For real-time alignment prior to image acquisition, a lower power of ~30 μW was used. All experimental procedures and protocols were reviewed and approved by the UC Davis Institutional Review Board (IRB).

2.3. Noise characterization for supercontinuum light sources

Given the limited available signal for visible light OCT, optimization of detection sensitivity is particularly important. In a SC light source, amplified shot noise during generation of a large optical bandwidth [27] results in higher relative intensity noise than superluminescent diodes, which are routinely used in commercial systems. The excess intensity noise, caused by pulse-to-pulse variability in energy and spectrum, can be mitigated by averaging more pulses through either increasing the pulse repetition rate or the detector integration time. To explore this parameter space, characterization of the shot noise, detector noise, and excess noise over a range of exposure periods was performed for two SC light sources with different pulse repetition rates.

An ideal heterodyne system operates in the shot noise limit, wherein the dominant noise source is based on Poisson distributed photoelectron counts. In general, there are three main additive sources of noise. The first, representing the detector noise (i.e. read noise and dark noise), has a variance independent of the number of detected photons, or photoelectrons, but possibly related to operating temperature. The second, representing shot noise, originates from the fundamental quantum noise in the number of photons detected. Shot noise has a variance equal to the number of detected photons, as dictated by Poisson statistics. The third, representing excess noise, originates from intensity fluctuations of the light source, and has a variance proportional to the square of the number of detected photons. Hence, the total noise variance of the OCT system σ^2 , in units of counts^2, can be described by the following expression:

$$\sigma^2[p(\lambda), \lambda] = a(\lambda) + b(\lambda)p(\lambda) + c(\lambda)p^2(\lambda) \quad (1)$$

in which $p(\lambda)$ is the number of detected counts and $a(\lambda)$, $b(\lambda)$, and $c(\lambda)$ are coefficients related to the aforementioned detector noise, shot noise, and excess noise (Note that $b(\lambda) = 1$ for Poisson statistics).

The noise performance of a low noise SC light source from NKT Photonics, the EXU3, was

Biomedical Optics EXPRESS

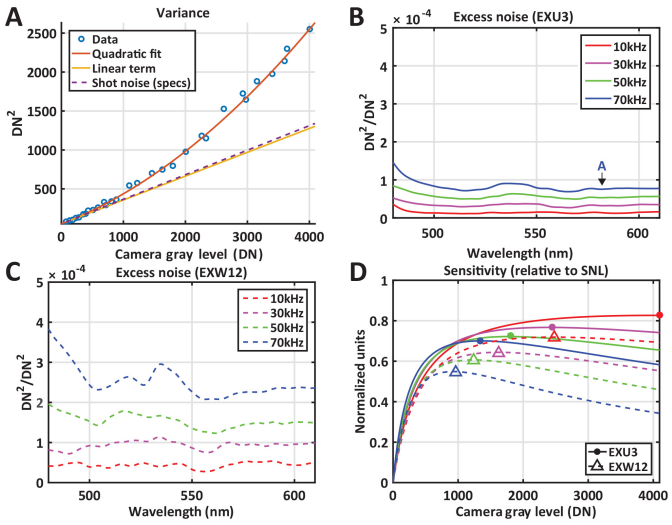

Fig. 2. Noise analysis for two supercontinuum light sources, EXU3 and EXW12, at visible wavelengths. (A) Quadratic fitting of the total noise variance versus camera gray level (DN), where the linear term corresponding to shot noise (solid yellow line), agrees with shot noise predicted from the manufacturer specified responsivity of ~13000 counts / 4096 DN (dashed purple line). (B) The excess noise coefficient, $c(\lambda)$, of the EXU3, across visible wavelengths and a range of line rates, is shown, with an arrow indicating the location of the data in A. (C) The excess noise coefficient, $c(\lambda)$, of the EXW12 is ≥ 2x larger than that of the EXU3 at the same wavelength and line rate. (D) Due to reduced excess noise of the higher repetition rate EXU3 source, more reference counts can be used without introducing excess noise, enabling maximal sensitivities (filled circles) closer to the shot noise limit (SNL), and higher than those achieved with the EXW12 source (open triangles).

compared against its predecessor, the EXW12. The pulse repetition rate of the EXU3, f_{rep}, is 156 MHz, twice that of the EXW12 (f_{rep} = 78 MHz). Assuming independent pulses, doubling the repetition rate should halve the excess noise coefficient, $c(\lambda)$. To test this, based on the noise model in Equation (1), by varying the number of detected photon counts during the camera exposure, and analyzing the corresponding count variances at each pixel in the spectrometer, coefficients $a(\lambda)$, $b(\lambda)$, and $c(\lambda)$, with units of counts^2, counts, and dimensionless, respectively, were determined. Specifically, the temporal variance (in units of counts^2) was measured at each λ, or pixel, and the average photoelectron count $p(\lambda)$ was determined after dark count correction. The incident photon count was modified using a variable ND filter, and ~ 40 different average photoelectron count levels, albeit different for each camera pixel, or λ, were acquired. For each λ, 51,200 samples were used to assess the mean and variance. This multi-dimensional data set enabled fitting three λ- (or pixel-) dependent coefficients describing temporal noise contributions; a constant (independent of photoelectron count), $a(\lambda)$, a linear coefficient $b(\lambda)$ multiplying photoelectron count, representing shot noise, and a quadratic coefficient $c(\lambda)$, multiplying photoelectron count squared, representing excess noise, as shown in Fig. 2(A). Note that Fig. 2 uses units of camera gray levels (DN), with ~13000 counts / 4096 DN, and linear responsivity was assumed. The camera was operated without active cooling. When fitting three coefficients per pixel, the constant coefficient $a(\lambda)$ was found to be approximately equal to the dark count variance (the variance with no incident photons or $p(\lambda) = 0$) and the linear coefficient $b(\lambda)$ was found to be approximately equal to unity, as expected from Poisson statistics. In Fig. 2(B)-(C), the quadratic coefficient $c(\lambda)$ at four different acquisition line rates f_A (related to exposure period T_A by $f_A = 1/(T_A+T_d)$, where

Biomedical Optics EXPRESS

T_d = 2.1 μs) for both sources are presented, in which T_d is the camera dead (or readout) time. First, in both Fig. 2(B) and Fig. 2(C) the excess noise coefficient, $c(\lambda)$, increases noticeably at the short wavelength end of the spectrum near the cut-in wavelength [28]. Second, comparing Fig. 2(B) to Fig. 2(C), the excess noise level approximately halves as the repetition rate f_{rep} doubles, suggesting that $c \sim 1/f_{rep}$. Third, based on trends in Fig. 2(B) and Fig. 2(C) individually, the excess noise level decreases proportionately with increases in exposure period, $c \sim 1/T_A$. In summary, the data are consistent with $c \sim 1/f_{rep}T_A$, and excess noise is roughly inversely proportional to the pulse number during a camera exposure (i.e. $f_{rep}T_A$).

Given this detailed characterization of noise sources, the spectral dependence of noise variance can be determined for an arbitrary spectrum. Using measured spectra for both light sources, the sensitivity relative to the shot noise limit (SNL) as a function of camera peak gray level is plotted in Fig. 2(D) for both sources at a range of line rates. All plots show a maximum at the optimal gray level that enables sensitivity nearest to the SNL. In practice, to optimize sensitivity, the reference arm power can be set to achieve this gray level. In particular, reducing excess noise, either by increasing the pulse repetition rate or reducing the line rate, enables more reference gray levels to be used, in turn achieving sensitivities closer to the shot noise limit. Given these results, for the current study, the EXU3 light source was employed for retinal imaging at 10 kHz and 70 kHz line rates, with the reference arm gray levels set according to Fig. 2(D) to achieve sensitivities of ~83% and ~70% of the SNL, respectively.

3. Results

Alignment of subjects at low visible light power was performed using either an internal fixation, introduced via a dichroic illuminated by a red LED (Fig. 1(A)), or an external fixation, prior to image acquisition. Multiple safety mechanisms were built into the custom LabVIEW software, including laser power modulation, continuous galvanometer scanning, and laser shuttering, to ensure that the eye was not exposed to a stationary beam at any time during the imaging procedure. In addition, a low incident power of ~30 μW at the cornea was used for alignment and a switch incorporated in the software enabled the incident power to be raised to 150 μW for image acquisition. After image acquisition, illumination was shut down within 0.1 s using the shutter in the SC source controlled by the custom LabVIEW software. To compensate for differences between subject axial eye length and the 20 mm water cell (Fig. 1(A)), as well as fiber length mismatch between the arms, numerical dispersion compensation was applied to acquired images [29].

3.1. *In vivo* axial resolution

High-resolution *in vivo* human retinal images (configuration I) are shown in Fig. 3(A). The inner retinal layers as well as the 6 major bands of the outer retina are clearly resolved. The resolution *in vivo* was further verified based on analyzing a specular reflection from the inner limiting membrane (ILM). A window around the ILM consisting of 300 consecutive axial scans (red box in Fig. 3(A)) was first created. Then the complex data within the window were upsampled by a factor of 8 along the axial direction [30], and shifted so that the ILM peak was at the same axial position in each of the 300 scans. Next, the phase of each axial scan was uniformly corrected so that the phase at the ILM peak position was zero radians. Next, all 300 windowed axial scans, having been aligned and phase-corrected according to the ILM peak, were complex-averaged to yield a single ILM reflection profile, the amplitude of which is shown in Fig. 3(B). The full-width at half maximum of the reflection profile amplitude was ~1.78 μm (in tissue), at around 1/4 of the full axial imaging range, consistent with our system characterization (Fig. 1). Based on Fig. 1(E), a higher resolution is expected in the rest of the retina, which resides closer to the zero delay than the ILM in Fig. 3(A). On this basis, the conservative claim of *in vivo* retinal imaging with an axial resolution of < 2 μm in tissue is supported. After Fourier transformation of the complex

Biomedical Optics EXPRESS

ILM reflection profile, the spectral phase was unwrapped and finally, a first-order fit (constant plus linear term) was subtracted to yield the residual nonlinear phase. As shown in Fig. 3(C), the residual nonlinear phase was small compared to π radians, suggesting that dispersion and resampling errors were minimized, at least over the region shown in Fig. 3(A).

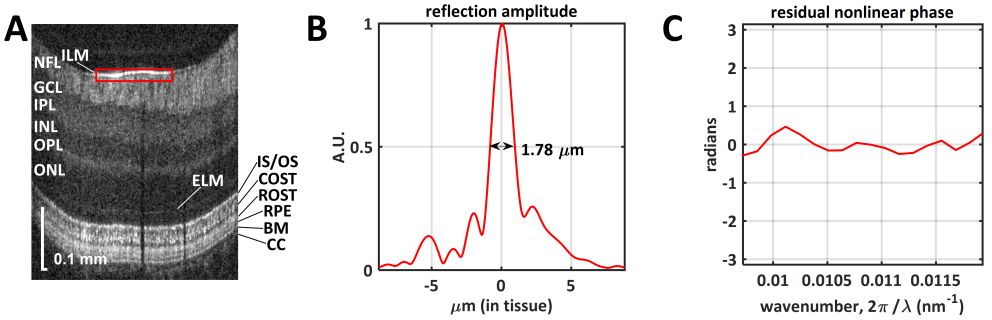

Fig. 3. (A) High resolution, *in vivo*, human retinal imaging. The nerve fiber layer (NFL), ganglion cell layer (GCL), inner plexiform layer (IPL), inner nuclear layer (INL), outer plexiform layer (OPL), and outer nuclear layer (ONL) are visualized in the inner retina. Outer retinal scattering bands include the external limiting membrane (ELM), photoreceptor inner/outer segment junction (IS/OS), cone outer segment tips (COST), rod outer segment tips (ROST), retinal pigment epithelium (RPE,) as well as Bruch's membrane (BM). Posterior to BM are the choriocapillaris (CC) and choroid, with reduced signal due to attenuation by pigment and blood. (B) Reflection amplitude for the inner limiting membrane (ILM), extracted from the window marked as red box in panel A. The full-width at half maximum (FWHM) of the reflection profile amplitude was ~1.78 μm in tissue, consistent with our measured axial resolution in air (Fig. 1(E)). (C) The residual nonlinear spectral phase of the reflection profile in panel (B) was small compared to π radians, suggesting that the dispersion and resampling errors were minimized. Imaging was performed using configuration I.

3.2. *High-definition retinal imaging*

In this section, high-definition retinal images acquired over a FOV of 13 mm (> 40°angular FOV) at an axial scan rate of 10 kHz (configurations II and III) are presented. As mentioned earlier, an incident power of 30 μW was used for real-time alignment mode, which facilitates adjustment of the optical path length mismatch, focus, fixation, as well as transverse beam placement on the pupil in order to optimize the image quality prior to acquisition at high power mode. Even at 30 μW, major retinal layers are visible (Fig. 4(A)).

Figure 4(B), an image at a comparable location of that in Fig. 4(A), but acquired at an incident power of 150 μW, is shown. As expected, higher signal-to-noise ratio (SNR) is achieved with better visualization of the ELM and outer retina. Using the same incident power of 150 μW, Fig. 4(C)-(E) shows images along or near the papillomacular axis. In Fig. 4(F), a zoom of the ROI labeled in Fig. 4(C) (red box) shows the RPE termination at the lamina cribrosa (LC). In Fig. 4(G), a zoom of the ROI labeled in Fig. 4(D) (blue box) shows the parafoveal and perifoveal regions with a visible posterior hyaloid membrane (PHM).

Biomedical Optics EXPRESS

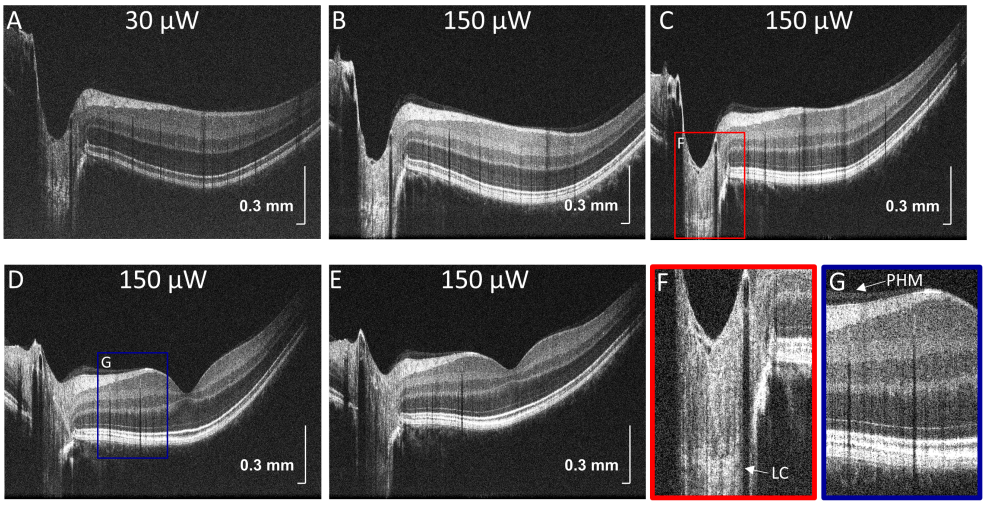

Fig. 4. High-definition images consisting of ~3800 axial scans over a field-of-view of 13 mm were acquired at an axial scan rate of 10 kHz. (A) Images with 30 μW incident power were used for alignment. (B) Once aligned, higher sensitivity images were acquired with 150 μW incident power to better delineate retinal anatomy. (C-E) Additional images on or near the papillomacular axis show inner and outer retinal layers, while zooms (F-G) show the lamina cribrosa (LC) and a visible posterior hyaloid membrane (PHM). The image in panel A was acquired using configuration II, and images in panels B-G were acquired using configuration III.

3.3. *High-speed imaging and compounding*

In Fig. 5, a series of images, each consisting of 492 axial scans over 3.2 mm, was acquired using configuration IV near the optic nerve head at an axial scan rate of 70 kHz, a speed comparable to commercial OCT systems. Sequential images were separated by 6.3 μm along the "slow" axis, perpendicular to the direction of image acquisition. Motion correction was accomplished by the following iterative method: the next image in the series was cross-correlated with the average of the prior images to determine its relative axial shift. This shift was then compensated by a complex FFT-based algorithm [30], applied along the axial direction, and a new compound average was formed, including the newly corrected image. The process was then repeated for the subsequent image in the series. This figure shows examples of compound images with N = 1, 2, 4, and 8 averages. Averaging clearly reduces image speckle and noise, leading to better delineation of layers. Beyond N = 8, a point of diminishing returns was reached, where little benefit was achieved from further speckle and noise reduction, and real anatomical differences between the individual images in the series became more apparent.

Biomedical Optics EXPRESS

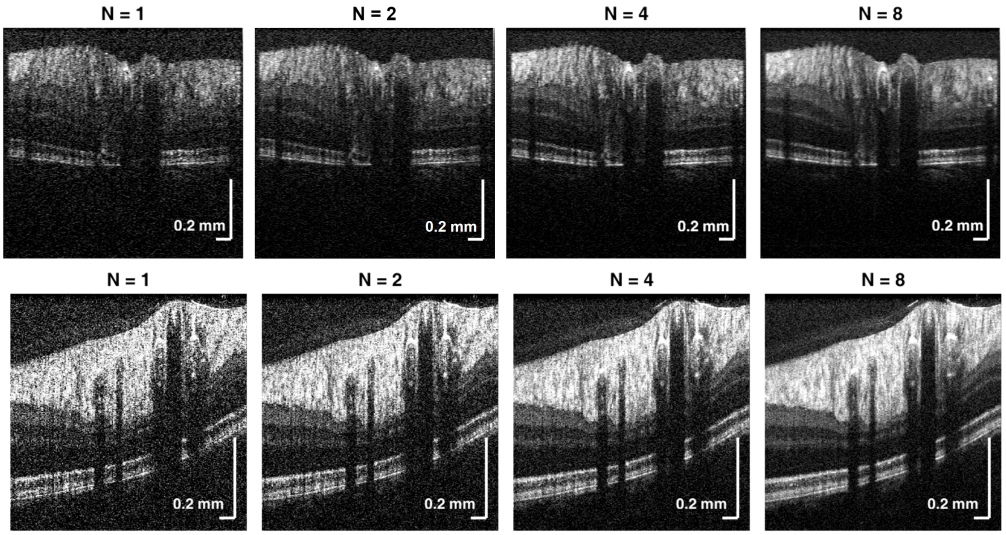

Fig. 5. Motion correction and averaging of images, acquired using configuration IV at a frame rate of 136 Hz, improves visualization of retinal layers. The images in the upper and lower panels, displayed on the same grayscale, were acquired at two different cross-sectional locations, superior and inferior to the optic nerve head, respectively. N is the number of images averaged.

3.4. *Split-spectrum spectroscopy*

The visible light reflectance spectrum of the retina is sensitive to both structure and biochemical composition. In this section, based on data acquired using configuration I, OCT retinal morphology is investigated with high resolution in two distinct regions of the visible light spectrum. The spectrum was first split into two non-overlapping sub-bands, centered at λ_c = 560 nm and λ_c = 620 nm, yielding FWHM axial resolutions of 4.0 μm in tissue for both sub-bands (verified by the ILM specular reflection as in Fig. 3). Each sub-band was processed and Fourier transformed to yield separate images, which were displayed in true color at their respective center wavelengths. Each image, defined as the magnitude squared or "intensity", was flattened to the IS / OS boundary (Fig. 6(A)). Then, each image was corrected for the noise bias. Next, each image was normalized to the strength of the specular reflection from the ILM. Finally, the squared magnitude was averaged, on a linear scale, over consecutive blocks of 50 axial scans in the transverse direction. Treating the mean of each block as an independent measurement, the mean signal (± s.e.m) was plotted on a logarithmic scale versus axial position (Fig. 6(B)). The inner retinal layers produced higher signal in the shorter wavelength sub-band, suggesting higher backscattering at shorter wavelengths. On the other hand, as shown in a linear scale zoom of the outer retina (Fig. 6(C)), the RPE and BM produced higher signal in the longer wavelength sub-band, possibly due to presence of chromophores such as melanin and photopigment that absorb more around 560 nm than around 620 nm.

Biomedical Optics EXPRESS

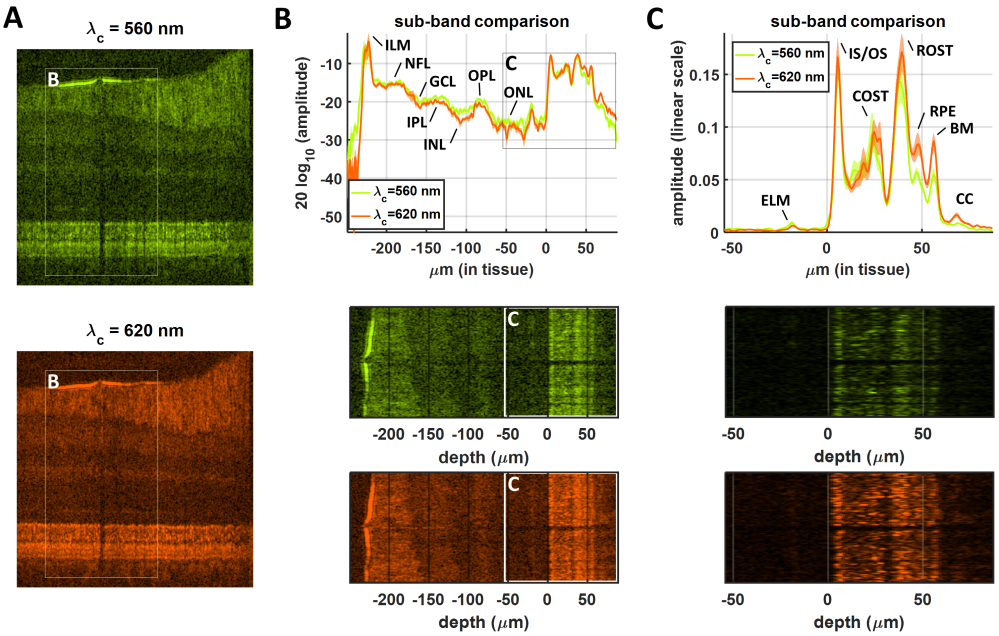

Fig. 6. Split-spectrum analysis of OCT retinal morphology. (A) Flattened sub-band images of the retina with center wavelengths of 560 nm (top) and 620 nm (bottom) are shown. The axial resolution was reduced to 4.0 μm (in tissue) within each sub-band, in exchange for spectroscopic information. (B) Axial signal profiles in each sub-band were normalized to the ILM reflection and averaged across a region of interest (white boxes in panel A), before plotting on a logarithmic scale. Interestingly, the inner retinal layers produced higher signal in the shorter wavelength sub-band, suggesting higher backscattering at shorter wavelengths. (C) Axial signal profiles of the outer retina, plotted on a linear scale, show that distinctive outer retinal layers can be visualized. The retinal pigment epithelium (RPE) and Bruch's Membrane (BM) produced higher signal in the longer wavelength sub-band, possibly due to presence of chromophores that absorb more around 560 nm than around 620 nm. Imaging was performed using configuration I.

Biomedical Optics EXPRESS

3.5. Doppler velocity, oxygenation and hematocrit mapping in vessels

In Fig. 7, an oversampled (~1900 axial scans, ~2 mm in lateral range) OCT retinal image acquired from a 35-year-old male using configuration I is shown. Doppler velocities, computed using a Kasai algorithm [31], and corresponding to axial motion of red blood cells (RBCs) in retinal vessels, are overlaid on the retinal image (Fig. 7(A)).

Using the spectroscopic fitting method described in [18], oxyhemoglobin (HbO_2) and deoxyhemoglobin (Hb) content of retinal vessels was estimated. Briefly, a noise bias-corrected absorbance spectrum was estimated using a sliding short-time Fourier transform (22 μm axial and 7 nm spectral resolution) of the complex OCT signal. An absorbance spectrum was determined by subtracting the logarithm of the noise bias-corrected intravascular spectrum from the logarithm of the noise bias-corrected spectrum of the inner retina (excluding the nerve fiber layer). The absorbance spectrum was fit (via linear least squares) using a model [18] that incorporated the effects of scattering and hemoglobin absorption, yielding path length times molar concentration, LC_{HbO_2} and LC_{Hb}.

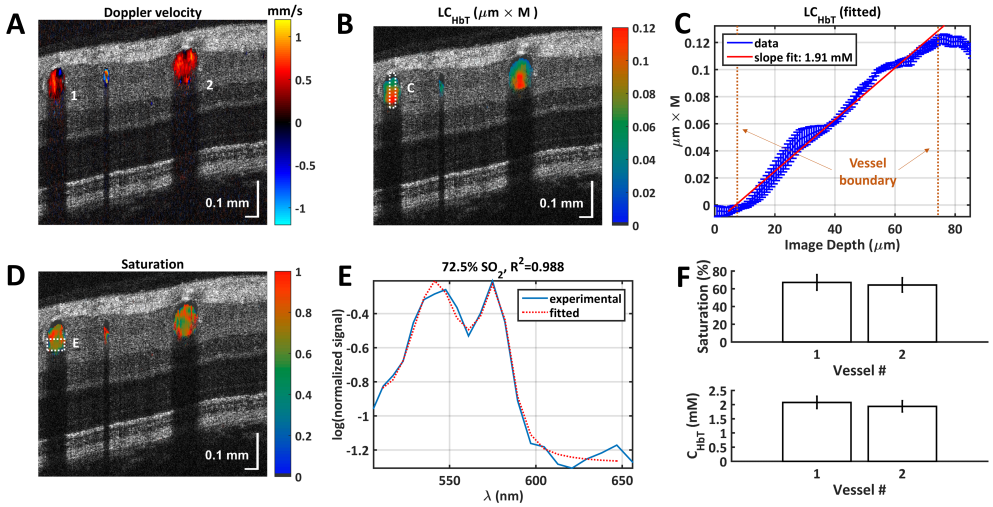

Fig. 7. Functional human retinal imaging using visible light OCT. (A) Image of Doppler velocities overlaid on structural OCT image. (B) Cumulative hemoglobin in retinal vessels exhibits a characteristic downward "crescent" shape, due to a larger cumulative path length at the distal end of the vessel. (C) The hemoglobin concentration in the marked vein was estimated to be 1.91 mM, corresponding to 12.3 g/dL. (D) Oxygen saturation mapping in retinal vessels is shown, with a spectroscopic fit for the distal portion of the vein (E). (F) The means and standard deviations of sO_2 and C_{HbT} are shown for vessels 1 and 2 (labelled in A) over a period of ~3 seconds. The measured saturations for the two vessels are 67.2 ± 8.8 % and 64.4 ± 8.2 % respectively. The measured C_{HbT} values for the same vessels are 2.08 ± 0.22 mM (13.4 ± 1.4 g/dL) and 1.94 ± 0.20 mM (12.5 ± 1.3 g/dL) respectively. Imaging was performed using configuration I.

Cumulative hemoglobin was determined from $LC_{HbT} = LC_{HbO_2} + LC_{Hb}$ (Fig. 7(B)). A hemoglobin concentration (C_{HbT}) of 1.91 mM (12.3 g /dL) was estimated from the marked vein in Fig. 7(B) based on the intravascular slope of LC_{HbT} (Fig. 7(C)). As an alternative approach, the fitted value of LC_{HbT} at the distal end of the vessel minus its value just proximal to the vessel, divided by the vessel diameter (L), yielded a C_{HbT} estimate of 1.86 mM (12.0 g/dL). Oxygen saturation (sO_2) was determined as $sO_2 = LC_{HbO_2} / LC_{HbT}$ (Fig. 7(D)). The sO_2 maps are thought to be most reliable at the distal ends of large vessels (Fig. 7(E)), where cumulative

Biomedical Optics EXPRESS

hemoglobin absorption and R^2 values are higher. The consistency of the saturation and C_{HbT} estimates of two vessels, labelled as '1' and '2' in Fig. 7(A), was assessed over a duration of ~3 seconds. The measured sO_2 values (Fig. 7(F), upper panel, mean ± std. dev.) for the two veins were 67.2 ± 8.8 % and 64.4 ± 8.2 % respectively. The measured C_{HbT} values (Fig. 7(F), lower panel, mean ± std. dev.) for the two veins were 2.08 ± 0.22 mM (13.4 ± 1.4 g/dL) and 1.94 ± 0.20 mM (12.5 ± 1.3 g/dL) respectively. The mean corpuscular hemoglobin concentration is 32 - 36 g/dL for human blood [32]. Thus, C_{HbT} in g/dL can be approximately converted to hematocrit in % by multiplying C_{HbT} by 3. Hence, corresponding hematocrit estimates are 40.3 ± 4.3% and 37.5 ± 3.9%, respectively.

4. Discussion

The current manuscript demonstrates a fiber-based visible light OCT ophthalmoscope for *in vivo* structural and functional imaging of the human retina.

4.1. Structural imaging

Permissible power levels for visible light are significantly lower than for near infrared light, and photon energies are higher, leading to smaller photon fluxes. Thus, the shot noise limit for sensitivity is lower for visible light. While this may be compensated to some degree by an increase in backscattering at shorter wavelengths (Fig. 6(B)), absorption (e.g. in the RPE as in Fig. 6(C)) and attenuation due to scattering (e.g. in the optic nerve head as in Fig. 4(F)) are also higher at visible wavelengths, leading to a very limited photon budget. Our results suggest that by optimizing the collection and detection efficiency, high quality imaging is nevertheless possible (Fig. 4). The sub-2 μm resolution in tissue achieved at visible wavelengths better highlights inner retinal striations (Fig. 4(C)-(E)) as well as outer retinal bands (Fig. 3(A)). At speeds comparable to commercial OCT systems, the speckle and noise in single images can be reduced through image compounding to improve visualization of retinal layers (Fig. 5). In spite of the high sensitivity, our results clearly confirm that visible light is not appropriate for imaging the choroid.

4.2. Spectroscopic imaging

Visible light OCT offers the prospect of functional imaging, as most retinal chromophores possess distinct absorption signatures at visible wavelengths. A key question that arises in spectroscopic imaging is how to account for the wavelength dependence of the transmittance of ocular media. For comparison of sub-bands, we normalized sub-band signals using the specular reflection from the inner limiting membrane (Fig. 6(B)). For hemoglobin fitting (Fig. 7(B)-(E)), a noise bias-corrected reference spectrum was derived from inner retinal tissue, excluding the NFL [33]. We anticipate that robust normalization strategies, perhaps differing according to chromophore, will be required for specific and quantitative measurements.

Both wavelength-dependent attenuation from scattering and wavelength-dependent backscattering are potential confounds in fitting hemoglobin concentrations. Our fitting algorithm, though previously validated *ex vivo* in calibrated rat blood samples [18], included neither wavelength-dependent nor saturation-dependent scattering effects [34]. However, we note that the reference spectrum normalization may help to compensate wavelength-dependent backscattering, if the reference tissue has similar backscattering properties to RBCs. Multiply forward scattered light is detected in our weakly confocal geometry, hence forward scattering events before or after a backscattering event from blood may not preclude detection. Nevertheless, we believe that more accurate hemoglobin estimates could be achieved by accounting for the dependence of scattering on wavelength and saturation in the fitting procedure.

Previous attempts at hematocrit quantification in the retina used the infrared OCT signal attenuation slope [35], which can be classified as a primarily empirical approach. Here, by fitting of absorbance using well-characterized hemoglobin absorption spectra, the hematocrit values

Biomedical Optics EXPRESS

for two retinal veins was determined to be slightly less than 40%. Though these values fall slightly below than the average systemic male hematocrit range of 40 - 45%, they are nevertheless physiologically plausible. Since hematocrit is split unevenly in downstream vessels [36], and microvasculature generally has a lower hematocrit, deviations from systemic hematocrit values in the retina can be expected.

4.3. Light exposure considerations

To minimize light exposure to the retina, a low power mode with only 0.03 mW at the cornea, yielding real-time images sufficient to optimize alignment, was employed prior to image acquisition with 0.15 mW. Besides enabling real time alignment, the capability to image the outer retina with low light flux may prevent photopigment bleaching in functional imaging studies. The capability to perform low power alignment is particularly important given the potential hazards of cumulative retinal exposure to visible light [21].

5. Conclusion

In conclusion, we described a multi-functional fiber-based visible light OCT system for human retinal imaging with < 2 μm axial resolution in tissue, and demonstrated *in vivo* imaging of Doppler velocity, hemoglobin saturation, and concentration, as well as spectroscopic imaging of the inner and outer retina with high resolution. These results suggest that visible light OCT is a promising avenue for future investigation, with potential advantages over near-infrared OCT for high-resolution structural and functional retinal imaging.

Funding

We acknowledge support from the Glaucoma Research Foundation Catalyst for a Cure, as well as the National Institutes of Health (R01NS094681).

Acknowledgments

We acknowledge Dawid Borycki, Tingwei Zhang, Yusufu Sulai, Alfredo Dubra, and Bradford Sohnlein for technical advice and general support.